*Journal of Marine Research, 57,* 471–502, 1999

# Salt fingers in three dimensions

**by Timour Radko[1] and Melvin E. Stern[1]**

ABSTRACT

Three dimensional (3D) numerical calculations are made for a vertically *unbounded* fluid with initially uniform vertical gradients of sugar ($S$) and salt ($T$), where $\tau = \kappa_S/\kappa_T = 1/3$ is the diffusivity ratio, and the molecular viscosity is $\nu \gg \kappa_T$. The latter inequality allows us to neglect the nonlinear term in the momentum equation, while retaining such terms in the *T-S* equations. The discrete 3D Fourier spectrum resolves the fastest growing horizontal wavelength, as well as the depth independent Fourier component. Unlike previous calculations for the pure 2D case the finite amplitude equilibration in 3D is primarily due to the instability of the lateral S-gradients in the fingers, and the consequent transfer of energy to vertical scales comparable with the finger width. It is shown that finite amplitude two-dimensional disturbances are unstable and give way to three dimensional fingers with much larger fluxes. Calculations are also made for rigid boundary conditions at $z = (0, L)$ in order to make a rough quantitative comparison with previous lab experiments wherein a finger layer of finite thickness is sandwiched between two well-mixed ($T$, $S$) reservoirs. The flux ratio is in good agreement, and the fluxes agree within a factor of two even though the thin interfacial boundary layer between the reservoir and the fingers is not quite rigid because sheared fingers pass through it. It is suggested that future experiments be directed toward the much simpler unbounded gradient model, for which flux and variance laws are given herein.

## 1. Introduction

This paper continues the calculation of Stern and Radko (1998, cited as "SR" hereafter) of the fluxes and statistics of salt finger in an unbounded ($x$, $y$, $z$) domain whose undisturbed state consists of vertically uniform property ($T$, $S$) gradients. Such a state has been realized in a "run-up" experiment using the "double bucket" technique to build up uniform property gradients from the bottom to the top of a tall vessel (Stern and Turner, 1969). This setup is significantly different (and conceptually simpler, as will appear) from the more common "run-down" experiments with two deep well-mixed layers with different ($T$, $S$) separated from the intervening finger region by a very thin transition region in which the fingers are sheared by the large-scale convective eddies in the mixed layer. This dynamically complex transition region may exert a "control" (or boundary condition) which limits both the amplitude of the vertical velocity in the finger region and its quantitative connection with the given ($T$, $S$) properties in the reservoirs. Also relevant (as

1. Department of Oceanography, The Florida State University, Tallahassee, Florida, 32306-4320, U.S.A.
***email: radko@ocean.fsu.edu***

mentioned in SR) is the fact that the past laboratory (4/3) flux laws are not generally applicable to oceanic salt fingers since deep homogeneous layers are seldomly observed at their extremities. In these cases the fluxes should be more directly related to the *locally* averaged $T$-$S$ gradient, by means of such relationships as obtained herein.

For reasons of tractability we consider the simplest parametric regime, one which is experimentally realizable and qualitatively (but not quantitatively) related to the oceanic case. This regime is the isothermal two-solute problem, where $S$ represents the contribution to the buoyancy of the lower diffusivity ($\kappa_S$) solute (e.g., sugar) and $T$ represents the higher diffusivity ($\kappa_T \equiv \kappa_S/\tau$) solute (e.g., salt). In this case ($\kappa_T \equiv 1.5 \times 10^{-5}$ cm$^2$/sec is small, compared to the viscosity $\nu \approx 1 \times 10^{-2}$ cm$^2$/sec, so that the finger Reynolds number $O(\kappa_T/\nu)$ is small, and the nonlinear *momentum* terms are negligible (SR) compared to buoyancy, viscous, and pressure gradient forces. This allows a great simplification in the numerical solution of the nonlinear thermodynamic equations for $dS/dt$, $dT/dt$. If the expansion or contraction coefficients in the equation of state is absorbed in the $(T, S)$ symbols, then the nondimensional $R = \overline{T}_Z/\overline{S}_Z$ gives the undisturbed vertical ($z$) density ratio, and the sugar finger experiments are encompassed in the parametric regime

$$R - 1 = O(1), \qquad \tau = k_S/k_T = O(1), \qquad 0 < \varepsilon \equiv \frac{1}{R\tau} - 1, \qquad \nu/\kappa_T \to \infty. \tag{1}$$

Previous 2D calculations (SR) have almost exclusively been used in the past. An exception is the work of Proctor and Holyer (1986) who conclude that for marginal finger convection with nearly *zero* growth rate the nonlinearly preferred mode is 2D and not 3D. This is in conflict with all laboratory experiments [without external shear] where 3D fingers are realized. In the present paper, on the other hand, the *fastest* growing wave is fully resolved at finite amplitude, and we will show that 2D fingers are unstable to 3D perturbations, even when the initial state 2D fingers consists of relatively large amplitude and chaotic structures. In Section 2d it is shown that the finite amplitude 3D motion consists of a chaotic horizontal planform containing a "mixture" of "square" cells and "rolls." The main quantitative result (Section 4) is that the vertical fluxes and horizontal variances in 3D fingers are much larger than in the 2D case, at least for the $R \geq 1.6$ range of the computations. The flux is primarily due to the dominant depth-independent Fourier mode, which equilibrates (Section 3c) by energy transfer to small vertical wavelengths; the modification of the horizontally averaged $T$, $S$ fields is unimportant in this model which is spatially homogeneous in the statistical sense.

Since our unbounded model has significantly different "end conditions" than previous laboratory experiments, we make calculations (Section 6) for *rigid* boundary conditions at $z = (0, L)$, where $T$ and $S$ are also prescribed, and where very thin *purely* diffusive boundary layers also appear. In this case steady 3D fingers with square planform are obtained with a flux ratio in good agreement with the "reservoir" experiments, and the individual fluxes agree within a factor of two.

Asymptotic calculations for $\varepsilon \to 0$ and $\tau \to 0$ (Section 5) are also presented since these

support the mechanistic picture and explain dependence of the fluxes on the parameters $(\tau, R)$ obtained in the finite $(\varepsilon, \tau)$ calculations.

## 2. Calculations for moderate "aspect" ratio $\mu$

### *a. Formulation*

As in SR the Boussinesq equations of motion are nondimensionalized using the conventional "finger width" $d = (\kappa_T \nu / g\overline{T}_z)^{1/4}$ as the length scale; $\overline{T}_z d$ is the scale for both the total "temperature" deviation $(T'(x, y, z, t) + \theta(z, t))$ and the total "salinity" deviation $(S' + \sigma(z, t))$ from their respective undisturbed values $(\overline{T}, \overline{S})$; $\kappa_T/d$ is the velocity scale; $d^2/\kappa_T$ is the time scale, and $\nu\kappa_T/d^2$ is the pressure scale. By definition the horizontal average (denoted by a bar) of $T'$ and $S'$ vanishes. In the limit [Eq. (1)] appropriate to sugar-salt fingers the Boussinesq equations reduce to

$$\begin{cases} 0 = -\nabla p + \nabla^2 \mathbf{v} + (T' - S')\mathbf{k} & (2.1a) \\ \nabla \cdot \mathbf{v} = 0 & (2.1b) \\ \dfrac{d}{dt}[T' + \theta] + w = \nabla^2(T' + \theta), \qquad T \equiv T' + \theta & (2.1c) \\ \dfrac{d}{dt}[S' + \sigma] + \dfrac{1}{R} w = \tau\nabla^2(S' + \sigma), \qquad S \equiv S' + \sigma & (2.1d) \end{cases}$$

where $p$ is the departure of the pressure from the horizontal average. Two more "mean field" equations are the definitions of $\theta(z, t)$, $\sigma(z, t)$ as the horizontal averages of $(T, S)$. Alternatively, as in the Fourier series calculation given below, $(\theta, \sigma)$ appear as the zero vertical wave number components of $(T, S)$ in Eq. (2.1c,d).

In our unbounded $T$-$S$ field we introduce a finite computational domain which is periodic in $x$, $y$, and $z$. The vertical size of this is a large multiple $(\mu)^{-1}$ of the finger width, but the important depth independent Fourier mode $(m = 0)$ is included. The fundamental horizontal wavelength $(k_0)$ and its harmonics fully resolve the fastest growing wave, and its *sub*harmonic will be included in some calculations. These are first performed (Section 2) for $R = 2.8$ and for a moderate aspect ratio of $\mu = 1{:}5$, defined as the ratio of the horizontal finger wavelength to the maximum (finite) vertical wavelength. Subsequent (Section 3) calculations, extending to smaller aspect ratios: $1/10 < \mu < 1/80$ will demonstrate convergence of the statistics. In Section 4 the calculations are extended to smaller $R$ where the amplitudes are larger. Quantitative results for heat flux and temperature variance as a function of $R$ are given for the fixed $\tau = \frac{1}{3}$ appropriate to a sugar-salt laboratory experiment.

Eqs. (2.1a,b,c,d) will be integrated in time using a pseudo-spectral method, in which all the equations are inverted exactly in the Fourier space, and the aliasing error associated with differentiation in $z$ is removed by zero padding. The Fourier images of Eq. (2.1a,b) are then given by the linear relation

$$-\kappa^2 p_3 = im(T'_3 - S'_3),$$

where $A_3$ here denotes the Fourier amplitude of a quantity with wavenumbers $(k, l, m)$ and $\kappa^2 = k^2 + l^2 + m^2$. The advantage of the high Prandtl number equations is that the pressure anomaly is readily computed from the $(T, S)$ field, and then the velocities are determined by (2.1a). Time integration of Eq. (2.1c,d) performed by a fourth order Runge-Kutta scheme and a periodic Cartesian grid with $(N_x, N_y, N_z)$ points is used to compute the nonlinear terms. Periodic boundary conditions for $T = T' + \theta$ and $S = S' + \sigma$ in $x$, $y$, and $z$ appropriate for the Fourier-spectral method are employed, and the size of the computational domain is systematically increased (Section 3) as $\mu$ decreases, thereby approaching an *unbounded* fluid state.[2]

*b. Time-dependent solutions*

A 3D numerical calculation for the aspect ratio $\mu = 1/5$ was initialized with the fastest growing linear normal mode for $\tau = 1/3$, $R = 2.8$ (see SR). The first experiment was initialized using "rolls":

$$T' = 0.2 \sin(mz) \cos(kx + ly), \tag{2.2}$$

for the horizontal planform, and the second one using "square" cells:

$$T' = 0.2 \sin(mz) \cos(kx) \cos(ly), \tag{2.3}$$

where $k = l = k_0/\sqrt{2}$, $m/k_0 = 0.2$, and

$$k_0 = \left(\frac{\varepsilon}{3}\right)^{1/4}, \qquad \varepsilon = \frac{1}{R\tau} - 1. \tag{2.4}$$

Although this value of $k_0$ corresponds to the maximum growth rate (SR) for *long* waves $(m/k_0 \to 0)$, it is also close to the fastest growing horizontal wavelength for the finite $m$ given above. In both experiments [(2.2), (2.3)] the nondimensional time step was 0.1, a grid with $(N_x, N_y, N_z) = 8 \times 8 \times 32$ nodes was used, and the horizontal dimensions of the computational domain included one fastest growing wavelength $(2\pi/k_0)$.

For $0 < t < 100$ (Fig. 1) the disturbance (2.2) grows exponentially and the growth rate of $3.28 \times 10^{-3}$ is in acceptable agreement with the (linear) theoretical value $(3.58 \times 10^{-3})$, considering that the initial amplitude in (2.2) is not very small. The motion remains essentially two-dimensional until $t = 1{,}000$, at which time the three-dimensional noise (generated by the computer) is amplified by $(\overline{T}_Z, \overline{S}_Z)$, thereby producing the dramatic increase of the heat flux (Fig. 1) in the transition to the three dimensional time-dependent regime. At any time the horizontal cross-section (Fig. 2) of the typical $(T, S)$ field in this phase consists of irregular structures which are some combination of (3D) "square cells" and (2D) "rolls" (including their higher harmonics), as constrained by the limited $x$, $y$

2. Some comparisons were made using the integrating factor technique (Canuto *et al.,* 1987) to evaluate the linear diffusive terms, and this method proved superior for small $R$ (Section 4) where it allowed a larger $\Delta t$ (for computational stability). But for $R = 2.8$ (in this section) the two methods required the same $\Delta t$, and the results obtained by the two different methods agreed exceptionally well.

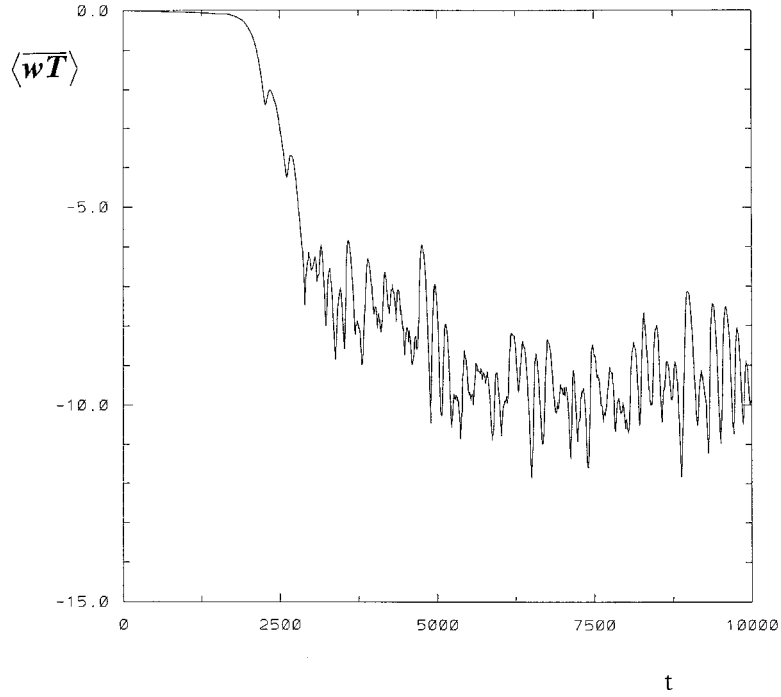


Figure 1. Numerical solution of the three-dimensional high Prandtl number equations for 1:5 aspect ratio, initiated by the 2D normal mode (Eq. 2.2). The average heat flux (Nusset number) is plotted as a function of time. By $t = 4{,}000$ heat flux reaches the statistical equilibrium value $Nu \approx 9$, as the system evolves to the time-dependent *three-dimensional* (see Fig. 2) chaotic regime. This instability is typical of all initial 2D conditions.

waves. The vertical cross-sections (Figs. 3a,b) indicate the dominance of the depth-independent ($m = 0$) harmonic, and the presence of smaller scales with comparable vertical and horizontal dimensions (referred to as "round eddies"). The perturbation density field (Fig. 3c), however, is not dominated by the $m = 0$ component, but by the "round eddies." Similar results have been obtained (not shown) with other initial conditions, such as the normal mode "square cells" (Eq. 2.3).

As in SR 2D case, it is possible to obtain 3D *steady* state solutions by using a code restricted to a sine series of Fourier components of ($T$, $S$). But when the resulting steady state [square cell] was used as an initial condition in an *unconstrained* 3D calculation (allowing for all the cosine terms including $m = 0$) an instability occurs, and the amplitude of the heat flux (not shown) increased dramatically; at $t = 4{,}000$ its value $Nu = 9$ was more than two orders of magnitude larger than in the constrained steady state. The structure of the resulting ($T$, $S$) field (not shown), as well as the statistically steady value of the heat flux, is similar to that obtained previously [in Figs. 1–3]: most of the energy is again in the $m = 0$ vertical mode, and the horizontal cross-sections reveal the complexity and irregularity of the planform. Results similar to those above have also been obtained using smaller

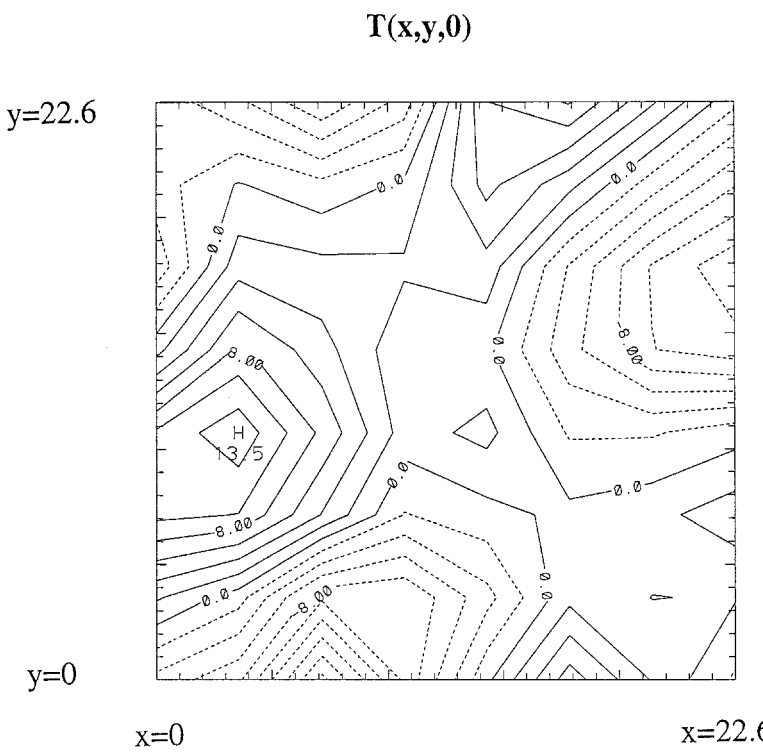


Figure 2. The isopleths of the temperature $T(x, y, 0, 10000)$ for the run in Figure 1 in a horizontal cross-section at $z = 0$. This illustrates the complexity of the three-dimensional $(T, S)$ field in the chaotic phase of the calculation.

computational domains with 1:4 and 1:2 aspect ratios (not shown); the latter calculation suggests that the character of the system might be captured by a "low-dimensional model."

*c. Subharmonic instability*

To determine the effects of the horizontal subharmonics with smaller wave numbers $(k/2, l/2)$ than the one of maximum growth, the following modification was made. The final data ($t = 7{,}500$) for the previous run were used as the initial condition in a computational domain twice as large (in both $x$ and $y$) as the one previously used. This horizontal grid contains *two* wavelengths of the fastest growing mode, and the initial condition contained a small amplitude subharmonic ($k_f = l_f = k_0/(2\sqrt{2})$). This has the surprising effect of reducing the heat flux to a new stable average (not shown) which is half the value that occurs in the absence of the subharmonic. The horizontal cross-section of the resulting $T$ field (Fig. 4) still indicates the dominance of the fastest growing mode, and the vertical cross-section (not shown) shows that the motion is still almost depth-independent.

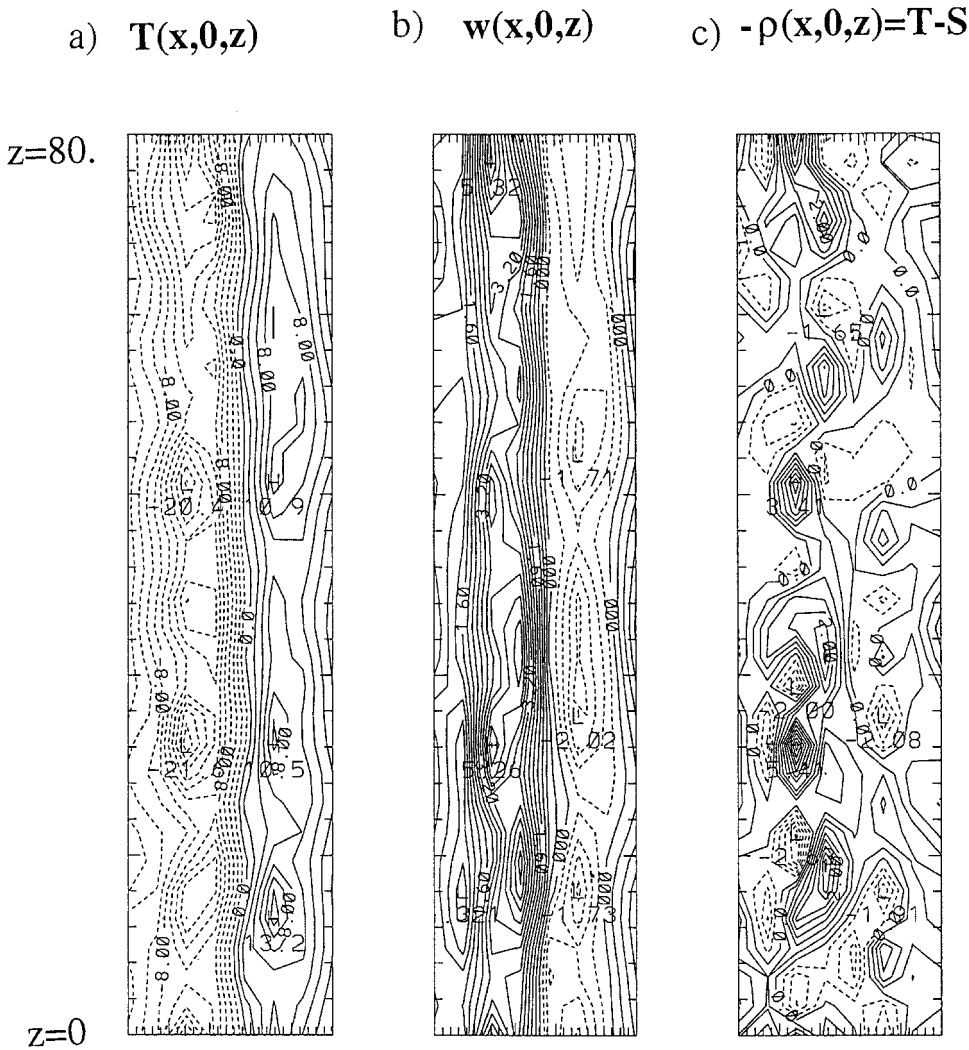


Figure 3. Vertical $(x, z)$ cross-section of (a) temperature $T(x, 0, z)$; (b) vertical velocity $w(x, 0, z)$; (c) density $-\rho(x, 0, z) = T - S$; for the run in Figure 1 ($t = 10{,}000$). The $m = 0$ mode dominates the amplitude of the temperature and the vertical velocity; this agrees with the well known visual signature of long, thin and "weak" ($R = 2.8$) fingers. The density plot emphasizes the presence of dynamically important perturbations whose vertical scale is comparable to the *width* of the salt fingers.

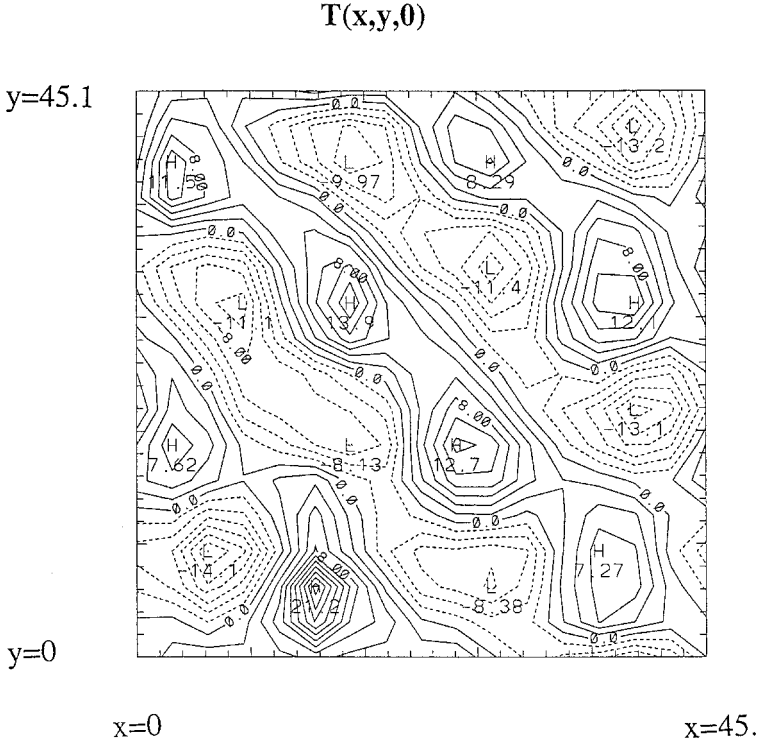


Figure 4. Horizontal cross-section of the temperature for the subharmonic calculation in Section 4c at $t = 2{,}000$ and $z = 0$. The isotherms indicate the dominance of the fastest growing mode, which here is half the fundamental Fourier wavelength, $\mu = 1/5$.

*d. Horizontal planform*

The horizontal planform in subsection b is limited geometrically by the fact that there are only two fastest growing modes in the Fourier expansion, these being associated with the orthogonal fundamental horizontal waves:

$$A \cos(kx + ly + \varphi_1), \qquad B \cos(kx - ly + \varphi_2), \tag{2.5}$$

where $A, B > 0$ and $k = 1 = k_0/\sqrt{2}$ from (2.4). All the previous calculations confirm that the largest amplitudes appear in these fastest growing modes (rather than their harmonics), so that the evolution of the horizontal planform of the salt fingers will yield either distorted "rolls" when $A \neq B$, or distorted "square cells" when $A \approx B$. Although this constraint is somewhat relaxed when the subharmonic is added (Fig. 4), one would really like to add waves with other azimuthal orientation. Nevertheless, some quantification of the planform structure can be obtained in terms of the parameter

$$\xi = \frac{A - B}{\sqrt{A^2 + B^2}},$$

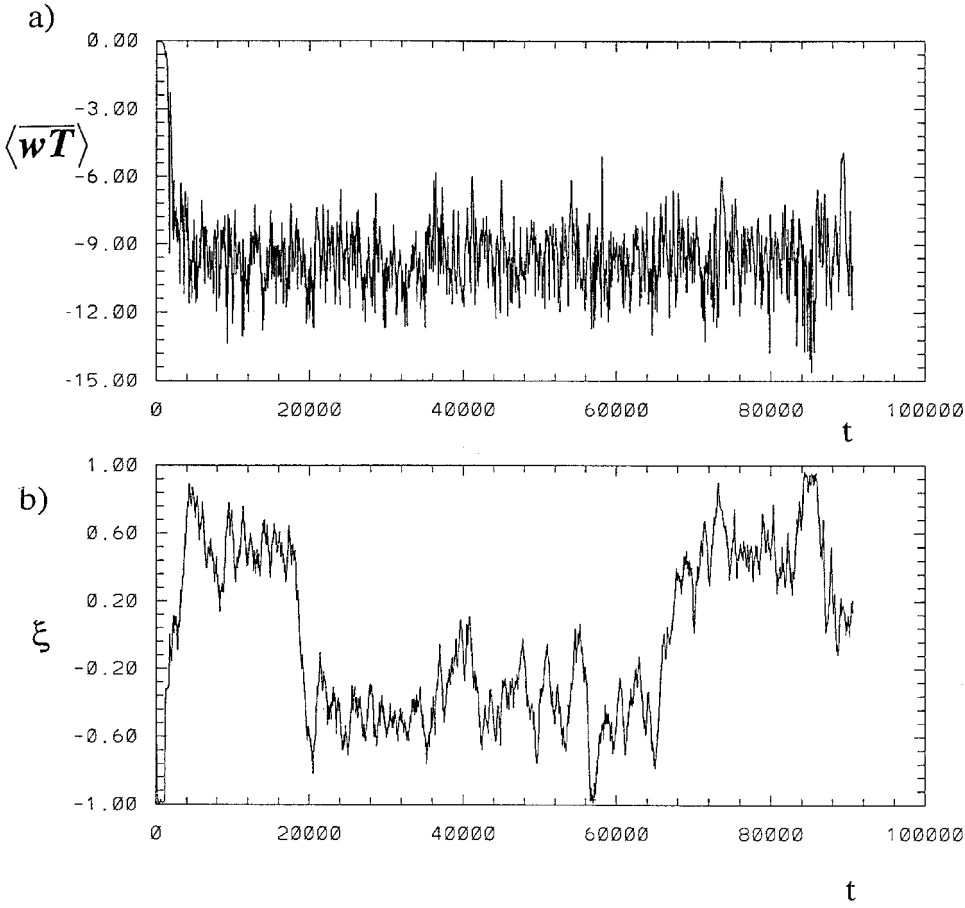


Figure 5. Destabilization of the exact "rolls" (see Appendix). (a) The heat flux as a function of time. (b) The parameter $\xi$, which indicates whether the state can be associated with the "rolls" ($\xi = \pm 1$) or with the "cells" $\xi = 0$. Note the presence of large time scales in the variation of $\xi$ reflects changes in *geometrical* orientation unaccompanied by heat flux. R = 2.8.

which indicates whether a particular field is mainly dominated by rolls in the $x - y =$ constant direction (when $\xi \to -1$), or by rolls in the $x + y =$ constant direction (when $\xi = +1$), or by square cells (when $\xi \to 0$). When this diagnostic was applied to the dominant $m = 0$ mode in Figure 2 the value $\xi = -0.64$ was obtained. In order to see how $\xi$ changes in time we considered the evolution of the steady-state "rolls" (see Appendix and Fig. 19a) when this state was used (without subharmonics) as an initial condition in an unconstrained three-dimensional run. Figure 5 shows that the heat flux reaches statistical equilibrium at $t = 4{,}000$ and then continuously oscillates about the mean value of $Nu \approx 9$, but the parameter $\xi$ exhibits oscillation on a remarkably larger time scale. The fastest growing disturbance (see Appendix) on the initial steady state consists mostly of orthogo-

nal rolls (in the $x - y =$ const direction), which explains the value of $\xi \approx -1$ near $t = 0$. Afterward the chaotic regime follows, wherein $\xi$ changes irregularly. Judging from Figure 5, the preferred (i.e., statistically more probable) values of $\xi$ are $\pm 0.5$, and the transitions between $\xi = 0.5$ and $\xi = -0.5$ regimes occur quite rapidly.

## 3. Smaller aspect ratios

In order to examine the effect of increasing the largest allowed (finite) vertical wavelength, the vertical size of the computational domain is now systematically increased. We shall see that very long waves do not have much effect for a certain range of $R$, and therefore the moderate aspect ratio calculations adequately describe the fluxes and variances in an unbounded fluid.

### *a. Convergence of the statistics*

We start with the $(T, S)$ field at $t = 12{,}650$ of the previous calculation (Fig. 5), and supplement this by a new and longer fundamental wavelength of $m = 0.1\ k_0$ with small initial amplitude. The vertical size of the computational domain was doubled by using 64 grid points in $z$ (instead of 32 employed previously). The resulting nondimensional heat flux (not shown) decreased from an average $Nu = 9$ to $Nu = 7$ units at the end of this run. The $T$-field ($\mu = 1/10$) in Figure 6 ($t = 2{,}000$ units after initialization) is similar to the final $T$-field for the $\mu = 1/5$ run in Figure 5, inasmuch as both are dominated in amplitude by the $m = 0$ harmonic (this is sometimes referred to as an *elevator mode*). The total disturbance "energy" $\langle \overline{T^2} \rangle$ of the state in Figure 6 is 39.5, while 38.0 of this amount is in the $m = 0$ mode, and these numbers are 25% less than those in the 1:5 case (for the run in Figure 5, $t = 12{,}650$). The distribution of the energy density (Fig. 7) for the $T$-field [similar in both cases] reveals two maxima: one of them is the fundamental wavelength and the other occurs around $m = 0.4$. Since the dominant *horizontal* wavenumber is also $k = 0.4$, this corresponds to our "round eddy" (see the short coherent waves in the region of large horizontal $T$-gradients in Fig. 6). In the next subsection we will show that these $m \approx k$ modes, *rather than the larger amplitude fundamental* or the mean field $\theta$, are the most important for equilibrating the (linear) growth of the large elevator ($m = 0$) mode.

Now we continue to decrease the aspect ratio by using the $(T, S)$ field for Figure 6 to initiate a new calculation with the fundamental wavenumber (in $z$) $m = 0.05\ k_0$, employing the same technique as used previously. After another $t = 2{,}000$ time interval the heat flux for this run (not shown) *increased* back to an average value of $Nu = 9$, and the oscillations of the heat flux became more regular. The energy spectrum is similar to that in the previous case, except that the magnitude of the fundamental harmonic ($m = 0.05\ k_0$) increases, and the latter feature persists when the calculations are extended to a $\mu = 1/40$ and then to a 1:80 aspect ratio (not shown). But the statistically averaged heat fluxes and the total energy do not change much when the aspect ratio is decreased as demonstrated by Table 1. The fact that the value of the energy density in the longest resolved harmonic ($m > 0$) increases as

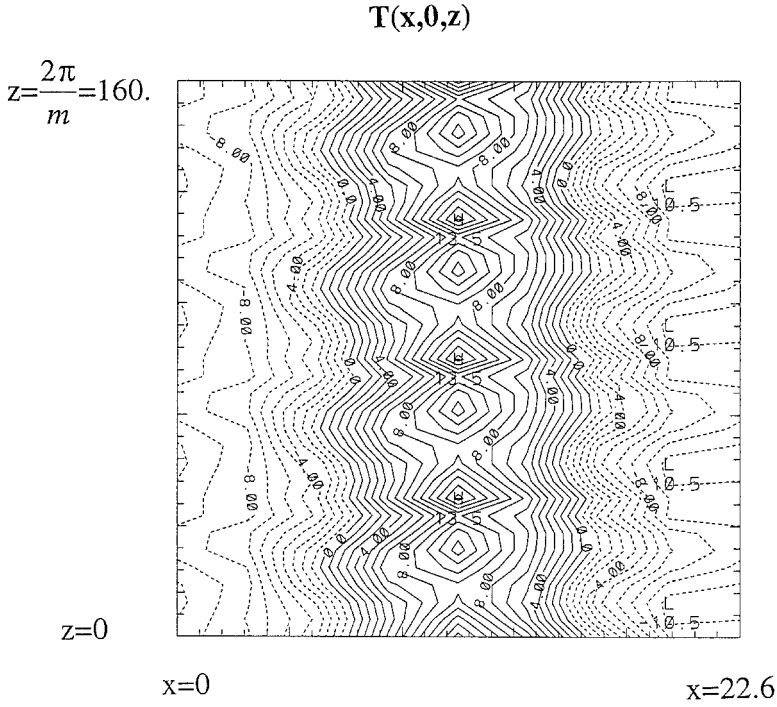


Figure 6. The isopleths of the temperature $T(x, 0, z, 2000)$ for the final state of the $\mu = 1/10$ run (see text). Note the coherent small-scale waves in the region of large horizontal $T$-gradients.

the aspect ratio is decreased, while at the same time the total energy in all the $m \neq 0$ modes does not change significantly suggests that the spectrum for the unbounded ($\mu \to 0$) system may have an *integrable* singularity at $m \to 0$.

To examine the effect of decreasing the aspect ratio in a *subharmonic* calculation we used ($T$, $S$) for the state in Figure 4 (*subharmonic* 1:5 calculation) and added a new and twice longer fundamental wavelength in $z$, using the same procedure as previously. When the calculation (not shown) was continued for 2,000 time units the heat flux or $Nu = 5.0$ was only slightly less than for the 1:5 calculation; the $T$-field at $t = 2{,}000$ and the $m$-spectrum were similar to those discussed above. The subharmonic calculations for $\mu = 1/20$ (Fig. 8) also gave similar results.

*b. Instability of chaotic 2D fingers*

As a final indication of the *ubiquitous* instability of 2D fingers we consider the *very chaotic* 2D state at $t = 10{,}000$ which SR obtained for $\mu = 1/20$, $R = 2.8$ using the initial condition

$$T = 0.2 \sin(k_0 x) \cos(2mz) + 0.02 \sin(k_0 x) \cos(mz) + 0.02 \sin((k_0/2)x) \cos(2mz).$$

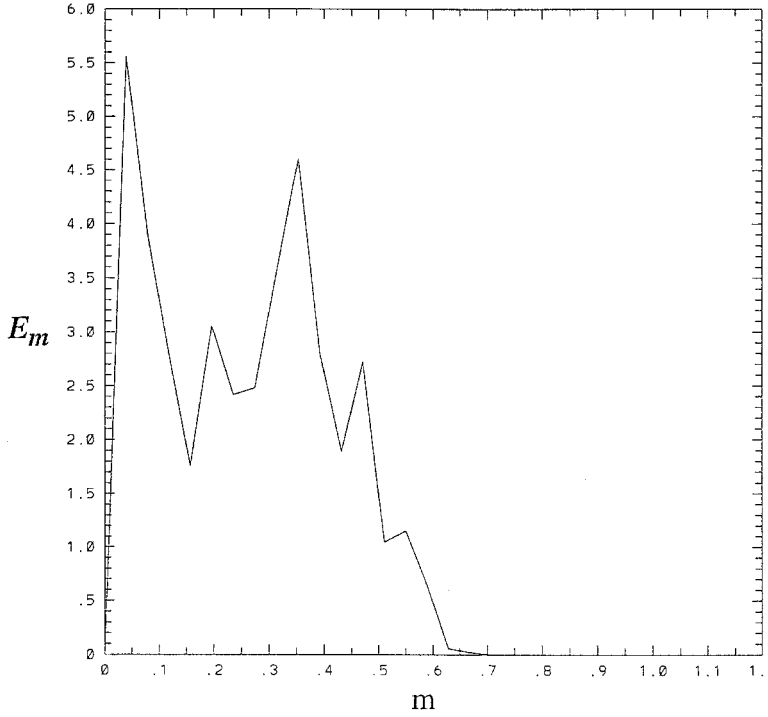


Figure 7. Distribution of the "energy" $\langle \overline{T^2} \rangle$ in vertical harmonics for the 1:10 aspect ratio state in Figure 6. The dominant $m = 0$ model is not shown. The spectrum has two maxima, one of which corresponds to the longest resolved wavelength and the other to the "round eddies" whose vertical dimensions are comparable with the finger width. The graph is normalized so that the area bounded by the curve corresponds to the energy in all the $m \neq 0$ modes.

The solution at $t = 10{,}000$ is now oriented as a role in the $x + y =$ constant direction, and then the calculation is continued using the *three-dimensional* code. Within the subsequent interval $0 < t < 500$ the $(T, S)$ fields (not shown) remain effectively two dimensional and the average value of the heat flux (Fig. 9) is close to the value of $Nu \approx 0.1$ obtained in the

Table 1. Heat flux, total energy $\langle \overline{T^2} \rangle$, and the part of energy contained in the $m \neq 0$ modes as a function of the aspect ratio. The latter two were obtained by averaging over several discrete times, whereas the heat flux is a complete time average. Note that neither heat flux nor the total energy change significantly as we decrease the aspect ratio.

| | | | $R = 2.8$ | | |
|---|---|---|---|---|---|
| | 1:5 | 1:10 | 1:20 | 1:40 | 1:80 |
| heat flux | 9.0 | 6.7 | 8.4 | 8.8 | 8.5 |
| total energy | 48.8 | 39.5 | 43.0 | 40.2 | 41.8 |
| energy in $m \neq 0$ modes | 2.7 | 1.5 | 2.1 | 2.5 | 2.5 |

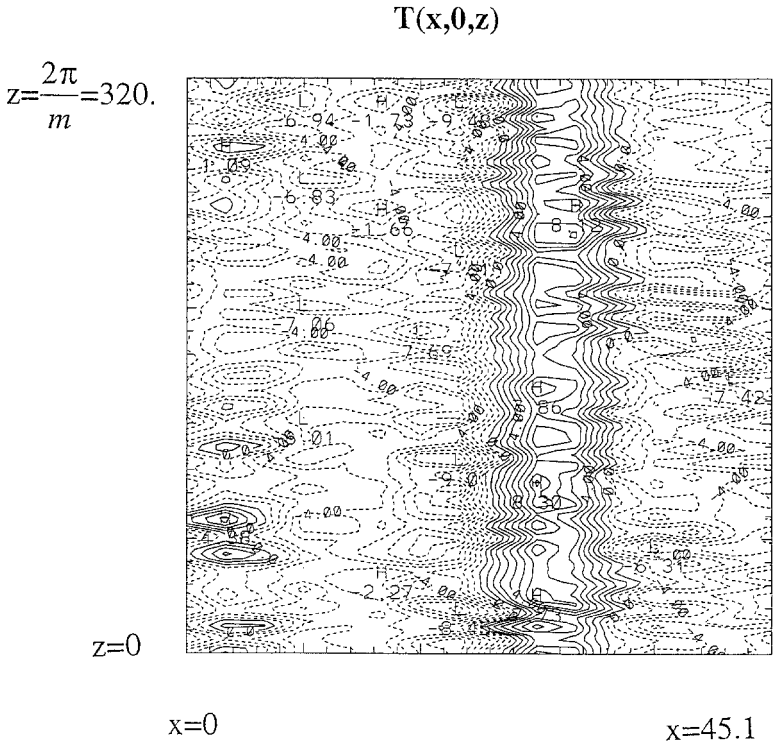


Figure 8. The isopleths of the temperature $T(x, 0, z, 1000)$ (the vertical cross-section) for the 1:20 aspect ratio run with subharmonics. Horizontal scale is exaggerated by a factor of $5\sqrt{2}$. The temperature field is dominated by $m = 0$ mode.

2D calculations, but at $t = 500$ the three-dimensional perturbations originating from numerical noise have grown sufficiently to affect the heat flux, and at $t = 3{,}300$ this increases by a factor of 50, at which level it starts to equilibrate. This agrees with the statistically steady value of $Nu \approx 5.0$ obtained above for the *subharmonic* calculations with quite different initial conditions.

*c. The mechanism of amplitude equilibration*

Why is the 3D heat flux much larger than the 2D flux, and what prevents the $m = 0$ normal mode from continually growing at the rate predicted by linear theory? One nonlinear stabilization mechanism, such as occurs in Rayleigh-Benard convection as well as in some constrained 2D salt finger calculations (SR), involves the modification of the horizontally averaged $T$, $S$ fields. To estimate the stabilizing influence of these terms, we reproduced some of our present calculations with a modified code in which the generation of these mean fields ($\theta$, $\sigma$) was suppressed by setting their value to zero at each time step. Remarkably, this alteration did not result in any significant changes in the statistically

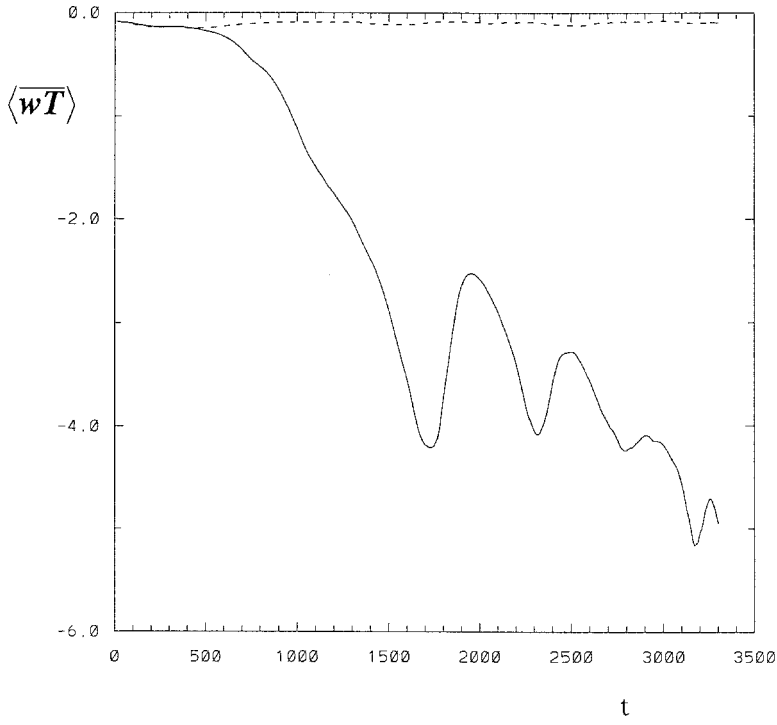


Figure 9. A highly disordered two-dimensional motion was used to initiate the three-dimensional calculations (solid line), in which the numerical noise grows rapidly and eventually result in the transition to the quite different regime, characterized by a larger heat flux. When these three-dimensional perturbations are numerically suppressed (dashed line) the heat flux remains small.

steady values of the heat flux and energy, and this proves that the $m = 0$ equilibration occurs by a different mechanism.

Another stabilization mechanism is by nonresonant (triad) energy transfer, e.g. mode $(k, l, m_1)$ interacting with $(2k, 2l, -m_1)$ draws energy from the self amplifying $(k, l, 0)$ mode. The magnitude of this energy transfer depends on the nonlinear heat advective term in the temperature equation:

$$N = \nabla \cdot (\underline{\mathbf{v}} T) = \nabla \cdot \left[ \sum_n \underline{\tilde{v}} \exp(inz) \cdot \sum_m \tilde{T} \exp(imz) \right], \tag{3.1}$$

where $\tilde{T}(x, y, m)$ is the Fourier transform (in $z$) of $T(x, y, z)$. The $z$-average of (3.1) can then be written as

$$N(x, y) = \sum_{n=1,M} N_{0n}(x, y) \tag{3.2}$$

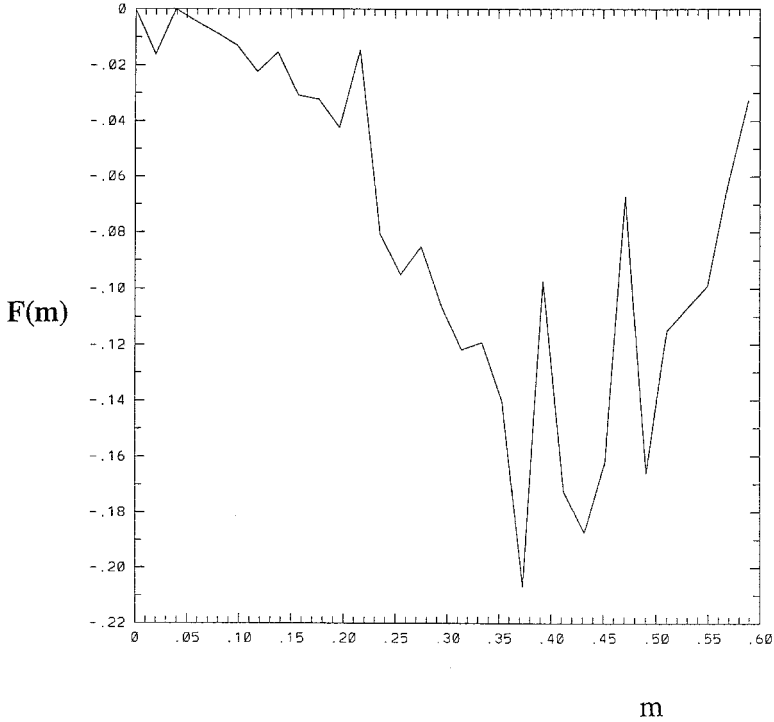


Figure 10. The energy transfer function $F(m)$ indicates the stabilizing effect of waves with different vertical wave numbers on the amplitude of the $m = 0$ mode (see text). The most effective in suppressing the growth of this mode are the "round eddies" ($m \sim 0.4$), area bounded by the curve corresponds to the total nonlinear transfer of the energy to the $m = 0$ mode (as in Eq. 3.3). The right-hand side of this equation was evaluated at equally spaced times in the 1:20 subharmonic run, and the results were averaged.

where $N_{0n}(x, y) = \nabla_h \cdot [\underline{\tilde{v}}(x, y, n)\tilde{T}(x, y, -n) + \underline{\tilde{v}}(x, y, -n)\tilde{T}(x, y, n)]$, and $M$ is the number of vertical harmonics. Then the equation for the $m = 0$ mode $[T_0(x, y)]$ is given by

$$\frac{\partial}{\partial t} T_0(x, y) = -\sum_{n} N_{0n}(x, y) + \text{linear contribution to } m = 0,$$

and the growth of its energy is

$$0.5 \frac{\partial}{\partial t} \overline{T_0^2(x, y)} = -\sum_{n} \overline{T_0(x, y) N_{0n}(x, y)} + \text{linear contribution}, \tag{3.3}$$

where the bar denotes an $(x, y)$ average. The plot (Fig. 10) of $F(m) = -\overline{T_0(x, y)N_{0n}(x, y)}$ as a function of $m = nm_0$ (here $m_0$ denotes the fundamental $z$ wavenumber) for the $\mu = 1/20$ subharmonic run demonstrates that the mode which is most effective in equilibrating (*via*

negative $F$) the $m = 0$ component has a vertical scale comparable to the horizontal one. This small-scale wave, easily visible in Figures 6 and 8, transfers heat and salt laterally ("eddy diffusivity") between up and downgoing fingers ($m = 0$). This, in conjunction with the lateral ($T$, $S$) gradients, equilibrates the growth of the fingers.

Figures 6 and 8 also suggest that these small-scale waves can be interpreted as instabilities of the *horizontal* temperature gradients associated with the $m = 0$ mode. Support for this view was obtained by an approximate linear stability calculation (not presented) using a "basic" state in which the vertical fingers were only growing slowly. Then the fastest growing new wave perturbation was found to have a scale consistent with the "round eddies" (i.e., $m \sim k_0$).[3] Since these have too small a value of $(m^2 + k_0^2)$ to draw energy from the undisturbed mean-field, it is quite plausible that their energy is supplied by the *horizontal* gradients in the "basic" salt fingers.

Why don't the longer waves ($m \leq 0.2$), with *larger* amplitude (see Fig. 7), have more of a stabilizing (eddy diffusivity) effect on $m = 0$ than the round eddies? One explanation is that the net *lateral* heat and salt flux, by the horizontal velocity ($u$, $v$) of the eddies is proportional to the small $\partial/\partial z \sim$ m, but this does not appear to be sufficient to account for the magnitude of the effect in Figure 10. Equally important is the phase correlation between ($T$, $S$) and $u$ or $v$; this correlation is apparently larger for the round eddies (see Figs. 6, 8) because of the energetics of the instability mechanism which produces them.

Relevant to this important point is the behavior of $F(m)$ in the two dimensional case, as was obtained from (SR) by averaging several $T$-files at $R = 2.8$. We then found (not shown) a tendency for equilibration ($F < 0$) of the $m = 0$ mode by the *long waves* (m $< 0.2$), and this implies that in 2D the longer waves of larger amplitude are more important than the round eddies, and these are able to limit the growth of $m = 0$ at lower amplitudes. This may be due to the fact that $\partial u/\partial x + \partial w/\partial z = 0$ in 2D in which case there is a direct correlation between $u$ and $w$ (or $T$) which results in a lateral $\overline{uT}$ flux. In 3D the $\overline{vT}$ flux in the long waves may have a compensating effect.

## 4. Extension to smaller R

After this rather extensive examination of the behavior of 3D fingers at one density ratio, we now proceed to values below $R = 2.8$. Since the calculations (Section 3) indicate that the averaged characteristics do not change as $\mu/k_0$ is decreased below 0.2, the following calculations are restricted to a 1:5 aspect ratio, and include a subharmonic component. As in SR, the calculations over a range of ($R$, $t$) were expedited as indicated below.

We used the state obtained at the end of the previous subharmonic run for $R = 2.8$, $\mu =$ ⅕ to initiate a new run with $R$ decreased to 2.6. Although the values of ($T$, $S$) at the grid-points were not changed, the spatial separation between the grid-points was decreased to reflect the modification of the $x$-wavelength of the fastest growing normal mode. The

3. A referee suggested these resemble the "lumpy" disturbances described by Turner and Chen (1974) in their Figure 3.

Table 2. Statistically steady values of the integral characteristics as a function of $R$. See text.

| Period of time | $R$ | $\Delta t$ | $-av\langle\overline{wT}\rangle$ | $av\langle\overline{T'^2}\rangle$ | $\gamma = \langle\overline{wT}\rangle/\langle\overline{wS}\rangle$ |
|---|---|---|---|---|---|
| 0–1,000 | 2.6 | 0.1 | 18.96 | 74.98 | 0.90 |
| 1,000–2,000 | 2.4 | 0.1 | 41.59 | 124.66 | 0.88 |
| 2,000–3,000 | 2.2 | 0.05 | 63.45 | 208.11 | 0.86 |
| 3,000–4,000 | 2.0 | 0.05 | 96.91 | 307.40 | 0.85 |
| 4,000–5,000 | 1.8 | 0.025 | 151.39 | 437.83 | 0.83 |

new calculation, carried on for an additional 1,000 time units, allowed us to obtain approximately statistically steady values of the heat flux and the temperature variance. Subsequently, $R$ was decreased four more times with initial values obtained in a similar manner, and the integral characteristics are summarized in Table 2. For the larger $R$ the time step employed was 0.1, but the smaller $R$ results in much larger amplitudes (Table 2), and numerical stability for $R = 1.8$ required a time step of 0.025.

Figure 11 reveals the temporal variation of average heat flux in each discrete $R$-interval, and the average in each interval is plotted in Figure 12 as a function of $ln\ \varepsilon$. Many structural features observed previously, such as the dominance of the $m = 0$ mode and the extreme disorder of the density field on the smaller vertical scales, appear in the low $R$ regime as well. Aside from the fact that the CPU time gets longer as $R$ decreases, the calculations are only recorded in Table 2 for $R \geq 1.8$ for the following reasons. At the end of the previous run for $\mu = 1/5$, $R = 1.8$ the code was modified to admit a much smaller ($\mu = 1/20$) aspect ratio, and then the run was continued for another 500 time units (not shown). During this interval there were fifteen oscillations of the heat flux about a mean value of $Nu = 120$,

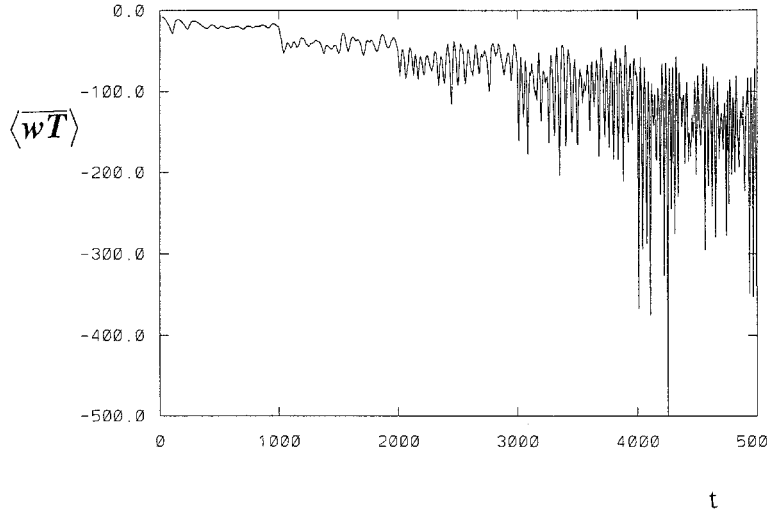


Figure 11. Variation of heat flux ($-Nu$) with t in discrete $R$ intervals (see text). $R = 2.6$ ($0 < t < 1000$), $R = 2.4$ ($1000 < t < 2000$). $R = 2.2$ ($2000 < t < 3000$), $R = 2.0$ ($3000 < t < 4000$), $R = 1.8$ ($4000 < t < 5000$).

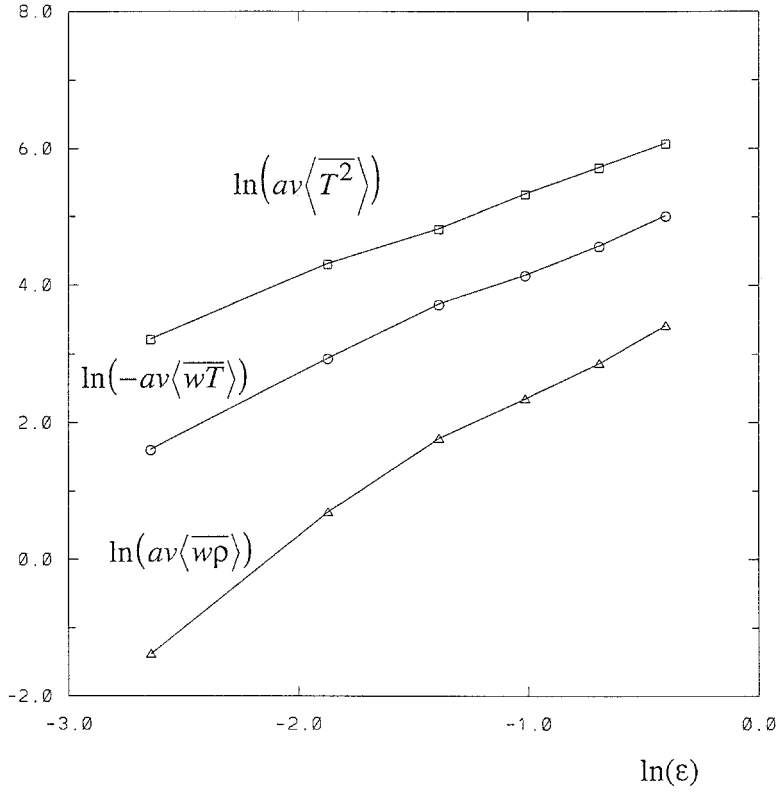


Figure 12. The statistical averages, obtained from the time records (e.g., Fig. 11) are plotted as a function of ε (in each segment) in logarithmic coordinates.

which is 25% less than the $\mu = 1/5$ value. Preliminary calculations for $R = 1.6$ indicated that the difference in *Nu* for $\mu = 1/20$ and $\mu = 1/5$ is even larger; i.e., the long waves which do not affect significantly the heat flux at $R > 1.8$ are becoming more important at smaller $R$. This can also be seen in Figure 13 where a long warm finger starts to fracture (near the bottom of the diagram) as a portion is sheared horizontally. Thus the regime ($R > 1.8$) of extraordinarily high vertical finger coherence is apparently changing to a new regime ($R < 1.8$), with more vertically irregular (fractured, bifurcated) fingers. On the other hand, the salt/heat flux ratio, as $R$ goes from 2.0 to 1.6, increases from 1/0.85 to 1/0.80 for *both* $\mu = 1/20$ and $\mu = 1/5$.

If the average heat flux, temperature variance and density flux are assumed to satisfy simple power laws of the form

$$-av\langle\overline{wT}\rangle = A\varepsilon^p, \qquad av\langle\overline{T^2}\rangle = B\varepsilon^q, \qquad av\langle\overline{w(T-S)}\rangle = C\varepsilon^r, \tag{4.1}$$

then the constants may be determined from the plot (Fig. 12) of the data in Table 2 and for

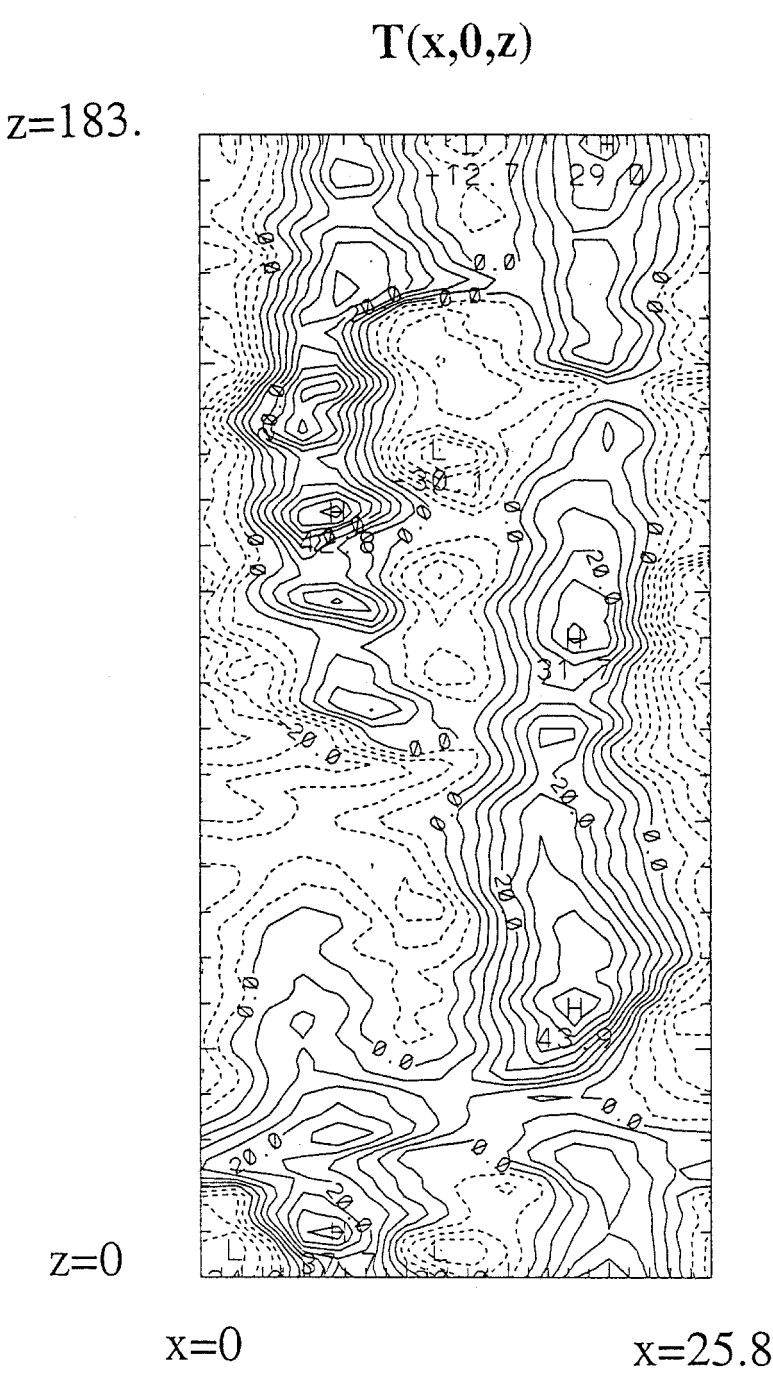


Figure 13. A vertical section of the isotherms ($T(x, 0, z)$ for $R = 1.8$ and a *small* aspect ratio 1:20 (the horizontal scale is enlarged by a factor of 3)). Note the "fracture" of the warm finger at the bottom, which is indicative of the onset of a regime ($R \leq 1.6$) in which the fingers have reduced vertical coherence.

$R = 2.8$ in Section 2. The least square fit of a straight line to this data yields

$$p \approx 1.50, \qquad q \approx 1.27, \qquad r \approx 2.11.$$
$$A = 291, \qquad B = 742, \qquad C = 84.$$

When the estimate of the slope of the curves is made from the two first points only (for $R = 2.8$ and $R = 2.6$), the values are:

$$p \approx 1.73, \qquad q \approx 1.43, \qquad r \approx 2.71.$$

The significance of these exponents appears in the following theoretical section, but the reader who is more interested in the relevance of the foregoing calculations to previous laboratory experiments may proceed to Section 6.

## 5. Asymptotic formulations

We shall now show that many of the foregoing features of salt fingers are retained in an asymptotic limit $\varepsilon \to 0$ ($R \to 1/\tau$), which simplifies the governing system (2.1) from two *T-S* prognostic equations to *one* first order equation (5.14), containing only *one* parameter ($\tau$). The results will supply confidence in the foregoing numerics and their physical interpretation. Moreover, the parametric range of this asymptotic theory is also experimentally realizable using different solutes, but this range ($\varepsilon \to 0$) is such that calculations using the more accurate equations (2.1) would be impractical. Asymptotic theory for $\tau \to 0$ (fixed $\varepsilon$) is also considered.

### *a. The nonlinear $\varepsilon \to 0$ equations with $\tau = O(1)$*

The linear theory (see Eq. 2.4) indicates that the *horizontal* wavelength of the fastest growing disturbance on the uniform ($T$, $S$) gradient is proportional to $\varepsilon^{-1/4}$, and for small $\varepsilon$ the growth rate of this perturbation is $O(\varepsilon^{3/2})$. This suggests transforming $x$ and $y$ using $\varepsilon^{-1/4}$ as the horizontal scale, and using $\varepsilon^{-3/2}$ as the time scale. Less obvious is the question of scaling the vertical coordinate $z$. Since the foregoing numerical calculations indicate that the "round eddies," with comparable horizontal and vertical dimensions are crucial for stabilizing the dominant $m = 0$ mode, we will also use $\varepsilon^{-1/4}$ as the vertical scale. (A much larger value of the latter was suggested by SR, but the following is the more appropriate $\varepsilon \to 0$ theory.) The continuity equation requires that the scales of all the velocity components $u$, $v$, and $w$ are the same.

Let us use the pressure $p$ as an independent variable and its scale is taken as $\varepsilon^{3/2}$ for the following reasons. The "density equation" formed by multiplying the salinity equation (2.1d) with $\tau^{-1}$ and subtracting the result from the temperature equation (2.1c) (as in Eq. 14 of Stern and Radko, 1998) results in a linear advection term $\varepsilon w$, and our previous work suggests that this is of the same order as nonlinear terms, such as $w(\partial/\partial z)T$. From this it follows that the scale of the temperature (and salinity) is $\varepsilon^{3/4}$. Since the diffusion term in (2.1c) is of the same order as the linear advective term we scale the velocity components as

$\varepsilon^{5/4}$. Finally, the momentum equation (2.1a) suggests that pressure term $\nabla p$ is of the same order as the viscous term $\nabla^2 v$, which implies scaling of the pressure as $\varepsilon^{3/2}$.

These anticipated balances lead to the following formal transformations of the variables in the temperature, salinity, momentum and continuity equations. Let

$$x = \varepsilon^{-1/4} x_0, \qquad y = \varepsilon^{-1/4} y_0, \qquad z = \varepsilon^{-1/4} z_0, \qquad t = \varepsilon^{-3/2} t_0 \tag{5.1}$$

$$(u, v, w) = \varepsilon^{5/4}(u_0, v_0, w_0) + \ldots, \qquad p = \varepsilon^{3/2} p_0, \tag{5.2}$$

$$T = \varepsilon^{3/4} T_0 + \ldots, \qquad S = \varepsilon^{3/4} S_0 + \ldots. \tag{5.3}$$

where (. . .) indicate higher order terms in the following expansion.

The result of taking the $\varepsilon \to 0$ limit is as follows. The leading order ($\varepsilon^{5/4}$) balance of the advection diffusion equations (2.1c,d) yields the *diagnostic* relationship

$$w_0 = \nabla_0^2 T_0 = \nabla_0^2 S_0, \tag{5.4}$$

where

$$\nabla_0^2 \equiv \frac{\partial^2}{\partial x_0^2} + \frac{\partial^2}{\partial y_0^2} + \frac{\partial^2}{\partial z_0^2}.$$

The physically important implication of (5.4) is that to leading order the *horizontal averages* ($\theta$, $\sigma$) of temperature and salinity are zero:

$$\overline{T}_0 = \overline{S}_0 = 0. \tag{5.5a}$$

Unlike the asymptotic expansion ($\varepsilon \to 0$) suggested by SR, these "mean field modification" terms are unimportant here. Eq. (5.4) also implies

$$T_0 = S_0. \tag{5.5b}$$

From the momentum equation (2.1a) we see that the scale of the next term in the expansion of ($T$, $S$) is $\varepsilon^{7/4}$; thus the expansion (5.3) should be continued as

$$T = \varepsilon^{3/4} T_0 + \varepsilon^{7/4} T_1, \qquad S = \varepsilon^{3/4} S_0 + \varepsilon^{7/4} S_1, \qquad w = \varepsilon^{5/4} w_0 + \varepsilon^{q} w_1, \tag{5.6}$$

where the as yet undetermined exponent $q$ needs to be evaluated (for consistency).

The leading order balance of the momentum equation (2.1a) gives

$$\frac{\partial}{\partial x_0} p_0 = \nabla_0^2 u_0, \qquad \frac{\partial}{\partial y_0} p_0 = \nabla_0^2 v_0, \tag{5.7}$$

and in view of (5.5b)

$$\frac{\partial}{\partial z_0} p_0 = \nabla_0^2 w + T_1 - \overline{T}_1 - (S_1 - \overline{S}_1), \tag{5.8}$$

wherein $\overline{p}_0 = 0$.

The next order ($\varepsilon^{9/4}$) balance of the advection diffusion equations (2.1c,d), using $1/R = \tau(1 + \varepsilon)$ gives the *prognostic* equations

$$\frac{\partial}{\partial t_0} T_0 + \nabla_0 \cdot (\mathbf{v}_0 T_0) = \nabla_0^2 T_1 - w_1 \varepsilon^q \tag{5.9}$$

$$\frac{\partial}{\partial t_0} S_0 + \nabla_0 \cdot (\mathbf{v}_0 S_0) + \tau w_0 = \tau \nabla_0^2 S_1 - \tau w_1 \varepsilon^q. \tag{5.10}$$

By subtracting from (5.9) and (5.10) their respective horizontal averages, bearing in mind that $\overline{T}_0 = \overline{S}_0 = 0$, we get

$$\frac{\partial}{\partial t_0} T_0 + \nabla_0 \cdot (\mathbf{v}_0 T_0) - \frac{\partial}{\partial z_0} (\overline{w_0 T_0}) = \nabla_0^2 (T_1 - \overline{T}_1) - w_1 \varepsilon^q \tag{5.11}$$

$$\frac{\partial}{\partial t_0} S_0 + \nabla_0 \cdot (\mathbf{v}_0 S_0) + \tau w_0 - \frac{\partial}{\partial z_0} (\overline{w_0 S_0}) = \tau \nabla_0^2 (S_1 - \overline{S}_1) - \tau w_1 \varepsilon^q \tag{5.12}$$

Now multiply (5.11) by $\tau$, subtract the result from (5.12), and use (5.8) to eliminate the right-hand side. Since $T_0 = S_0$, the result is

$$(1 - \tau)\left[\frac{\partial}{\partial t_0} T_0 + \nabla_0 \cdot (\mathbf{v}_0 T_0) - \frac{\partial}{\partial z_0} (\overline{w_0 T_0})\right] + \tau w_0 = \tau \nabla_0^2 \left(\nabla_0^2 w_0 - \frac{\partial}{\partial z_0} p_0\right). \tag{5.13}$$

For simplicity at this point we drop the subscripts "0" since all the following derivation is based on leading order variables. From (5.7), (5.4), and the continuity equation we obtain the diagnostic equation

$$\nabla_h^2 p \equiv \frac{\partial^2}{\partial x^2} p + \frac{\partial^2}{\partial y^2} p = -\frac{\partial}{\partial z} \nabla^2 w = -\frac{\partial}{\partial z} \nabla^4 T.$$

This results in the closed system of asymptotic equations:

$$\begin{cases} (1 - \tau)\left[\dfrac{\partial}{\partial t} T + \nabla \cdot (\mathbf{v} T) - \dfrac{\partial}{\partial z} (\overline{wT})\right] + \tau w = \tau \nabla^6 T - \tau \dfrac{\partial}{\partial z} \nabla^2 p & (5.14a) \\ \nabla_h^2 p = -\dfrac{\partial}{\partial z} \nabla^4 T & (5.14b) \\ \nabla^2 u = \dfrac{\partial}{\partial x} p & (5.14c) \\ \nabla^2 v = \dfrac{\partial}{\partial y} p & (5.14d) \\ w = \nabla^2 T & (5.14e) \end{cases}$$

in which the *only* nonlinear term $\nabla \cdot (\mathbf{v}T)$ available to equilibrate the growth of a (linear) normal mode requires the transfer of energy to two other Fourier components ("triad interaction"). These components are generally present in a noisy 3D system, but in a 2D flow there are special initial conditions (SR) where this is not the case, and in which the mean field terms $[(\overline{T}_0, \overline{S}_0) \neq 0]$ are required for equilibration. It only remains to indicate that the exponent $q$ (for the $w_1$ term) can be obtained by going to the next order in the prognostic equations (5.9–5.10), where we have terms like $\varepsilon^{7/4}(\partial S_1/\partial t_0)\, e^{3/2} + w_1\varepsilon^q$, from which $q = 13/4$ (in 5.6) is determined.

The asymptotic theory therefore suggests the following scalings of heat flux, temperature variance and density flux:

$$\langle \overline{wT} \rangle \sim \varepsilon^2, \qquad \langle \overline{T^2} \rangle \sim \varepsilon^{3/2}, \qquad \langle w(\overline{T - S}) \rangle \sim \varepsilon^{2.5}.$$

or in terms of notation used in Eq. (4.1) $p = 2$, $q = 1.5$, $r = 2.5$. Thus, the asymptotic theory rationalizes the empirical values $p = 1.73$, $q = 1.43$, $r = 2.71$ obtained numerically in Section 4.

*b. Numerical solutions of the $\varepsilon \to 0$ equations*

In that which follows we will numerically solve the asymptotic system of equations (5.14) and compare the qualitative results with the numerical solutions of the finite $\varepsilon$ system (2.1).

We again use a pseudo-spectral code for a periodic three dimensions grid with (8, 8, 32) points. The horizontal size of the computational domain was based on the wavelength of the fastest growing perturbation with no subharmonics permitted, and the aspect ratio was $m/k_0 = 1/5$. When initialized by a small amplitude two-dimensional normal mode $[T \sim \sin(k_0(x + y)/\sqrt{2}) \cos mz]$ of fastest growth, the motion soon became three-dimensional due to the instabilities originating from the numerical noise.

The variation of the heat flux in time is presented in Figure 14 in the "rescaled" variables [(5.1)–(5.3)], which are such that the previous heat flux ($Nu$) is related to the rescaled one ($Nu_0$) by $Nu = \varepsilon^2 Nu_0$. We can see that the system preserves the chaotic character of the finite $\varepsilon$ calculations, as well as the dominant amplitude of the $m = 0$ mode (Fig. 15). The vertical spectrum of the $T$-field (not shown) for $t = 250$ again reveals the importance of the round eddies ($m = 1$) for the equilibration of this $m = 0$ mode.

For quantitative comparison with the finite $\varepsilon$ calculation we note that a small finite $\varepsilon = 0.017$ gives an rms $T$ which exceeds the $\varepsilon \to 0$ result by 40%; this discrepancy is simply due to the fact that the nonlinear terms are still comparable to the linear ones even through $\varepsilon$ is so small.

*c. The asymptotic theory for $\tau \to 0$, $R \to \infty$, $\tau R = O(1)$*

For this limit we transform Eq. (2.1) by

$$t = (1/\tau)t_0, \qquad (u, v, w) = \tau(u_0, v_0, w_0), \qquad (T, S, p) = \tau(T_0, S_0, p_0), \qquad (5.15)$$

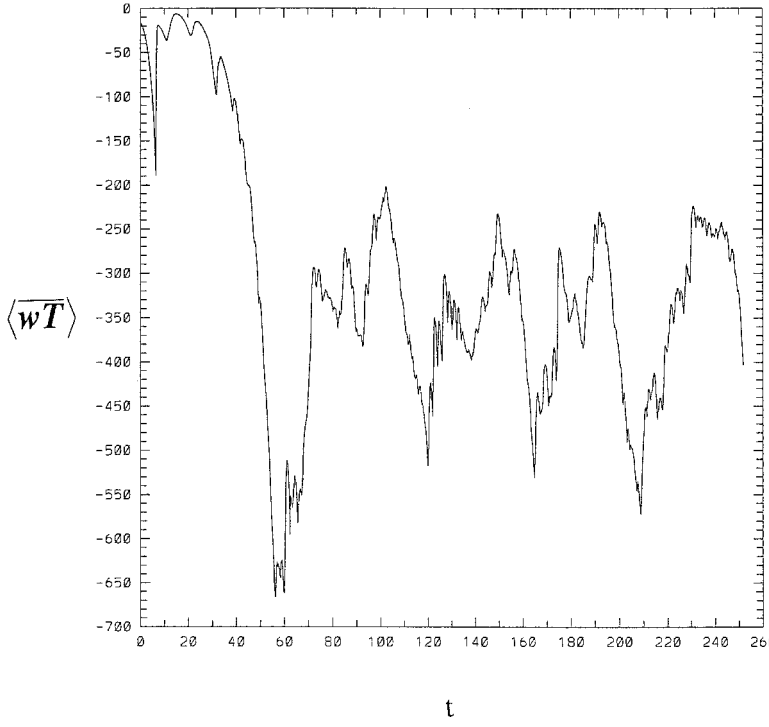


Figure 14. The heat flux as a function of time for $\varepsilon \to 0$ [Eqs. (5.14)]. The plot is in rescaled variables (see text). The 2D initial state evolves to a 3D chaotic regime with much larger flux.

and the resulting asymptotic ($\tau \to 0$) equations become

$$\begin{cases} 0 = -\nabla p + \nabla^2 \mathbf{v} + (\mathrm{T} - \mathrm{S}')k \\ \nabla \cdot \mathbf{v} = 0 \\ w = \nabla^2 T \\ \dfrac{\partial}{\partial t} S + \nabla \cdot (\mathbf{v}S) + \beta w = \nabla^2 S \end{cases} \tag{5.16}$$

where the subscripts "0" have been dropped.

Numerical calculations of these equations for $\beta = (\tau R)^{-1} = 1.071$ were initiated with the $t = 12{,}650$ data of the run in Figure 5 rescaled according to (5.15). Then the calculation was carried on using (5.16) for $t = 8{,}000$ (rescaled units), and the resulting heat flux eventually equilibrates at $Nu_0 \approx 150$, which gives

$$Nu \approx 150\tau^2 \ (\tau \to 0, \beta = 1.071). \tag{5.17}$$

The vertical cross-section of the final $S$-field (Fig. 16) again reveals the dominance of the $m = 0$ mode as well as the presence of the "round eddies" with the vertical wavenumbers $m \approx k_0$, and the horizontal cross-section (not shown) is dominated by the fundamental

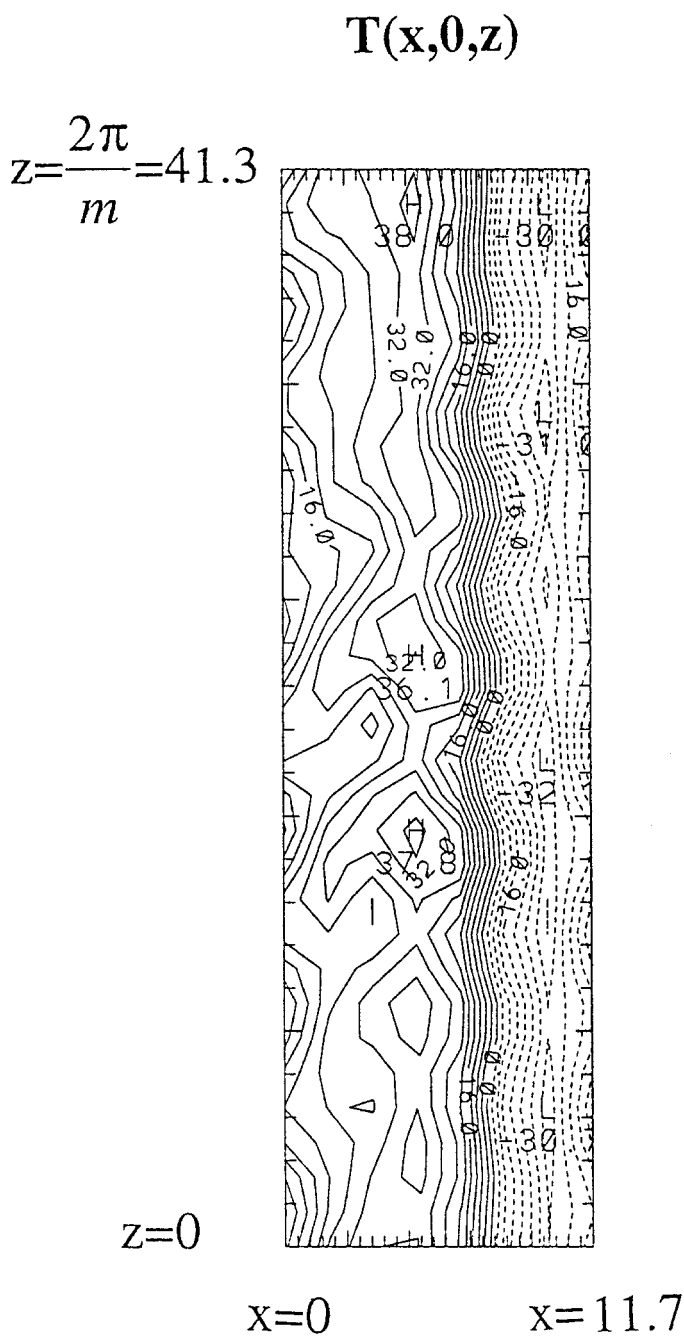


Figure 15. The isopleths at $t = 250$ of the temperature $T(x, 0, z)$ for the run in Figure 14. The motion is dominated by the $m = 0$ mode, and structure of the vertical cross-section is similar to those observed in the calculations with the finite ε code.

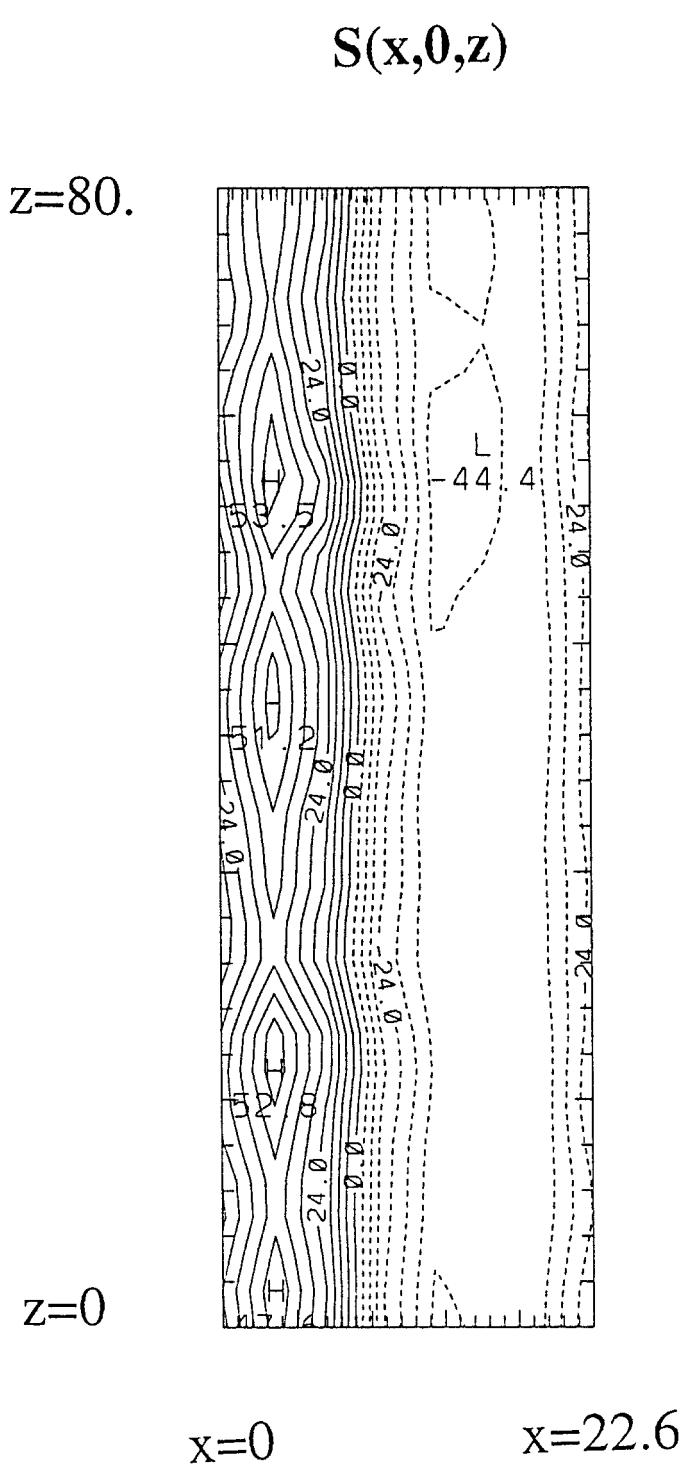

Figure 16. The isopleths of the salinity $S(x, 0, z, 8000)$ for Eq. (5.16). Note the dominance of the $m = 0$ mode and the presence of the smaller scale features. Structure of the salinity field is remarkably similar to that which was observed in the calculations with the finite $\tau$ system.

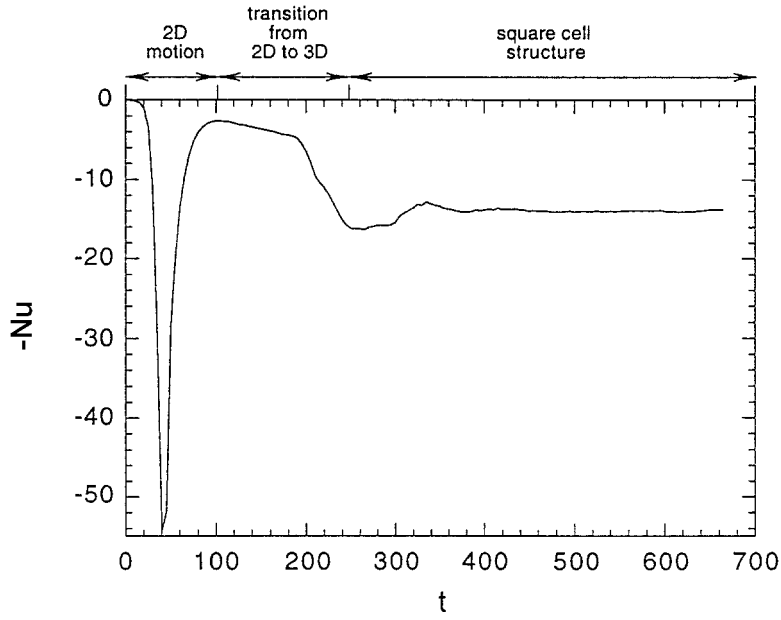


Figure 17. The heat flux as a function of time for a "rigid lid" experiment, the motion is initiated by 2D rolls which transform to the square cell structure as a result of the instability. (No subharmonic.)

(fastest growing) mode. All of these features are qualitatively similar to what was observed in the calculation with the original system (2.1). The quantitative error in the heat flux was 80%, relative to that in Figure 5 ($\tau = \frac{1}{3}$), but calculations using Eqs. (2.1) for $\tau = \frac{1}{6}$ with the same $\beta = (1/R\tau) = 1.071$ gave an average value of the heat flux which reduces the error of (5.17) to 45% as we decrease $\tau$ by a factor of two; this is consistent with the scaling of the relative error of our theory as $O(\tau)$.

## 6. Comparison with experiments

The only flux measurements available to compare with our low Reynolds number theory are in those "run-down" experiments in which the sugar fingers are coupled to deep convecting layers (with specified $T$, $S$) by very thin horizontal transition regions through which the sheared fingers pass. To some extent the very complex dynamics in the latter regions must control the maximum vertical velocity (and fluxes) in the finger layer. Since there is no such inhibition on $w$ in our unbounded model, we expect that the latter overestimates the flux relative to the "run-down" experiment, for a given value of $R$ in the finger layer. Additional calculations have, therefore, been made for *rigid* ($w = 0$) slippery conditions with specified ($T$, $S$) at $z = (0, L)$ in the expectation that this strong boundary condition will better model the "run-down" fluxes at the same $T$, $S$.

Figure 17 shows the nondimensional heat flux for an aspect ratio $\mu$ = finger half width/$L$ = 1/40 when $R = 1.6$, and when w is constrained to be a Fourier sine series ($w = 0$

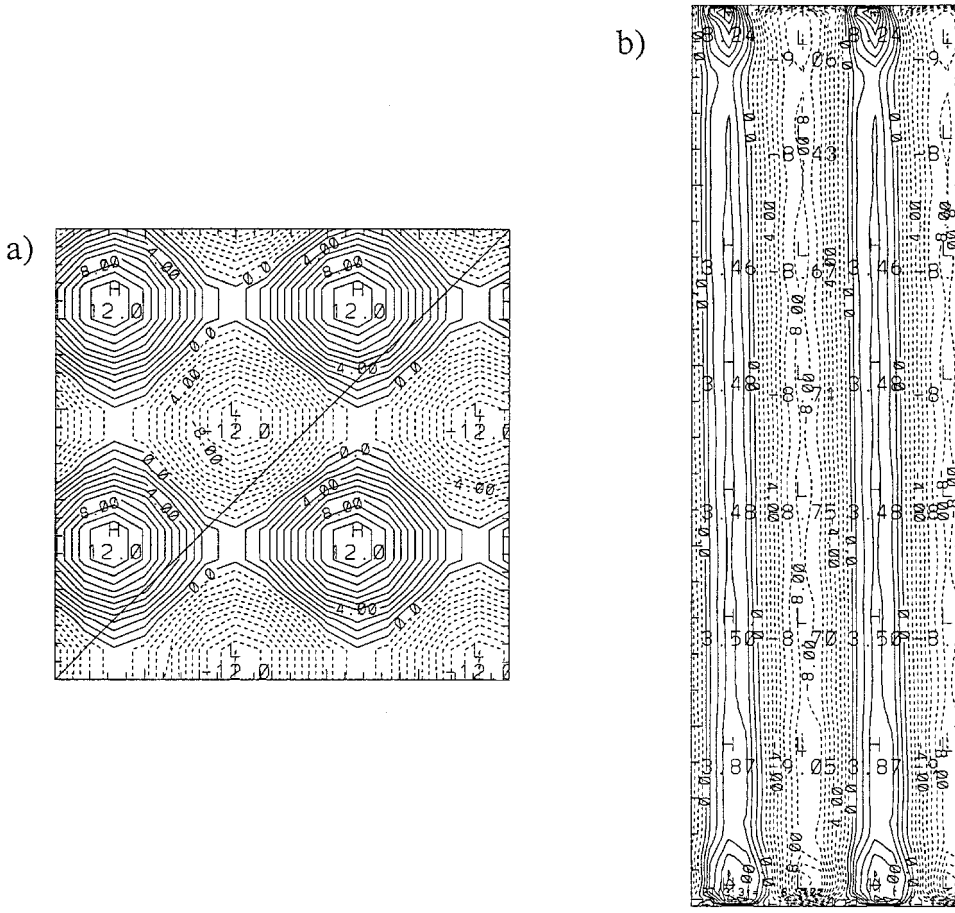


Figure 18. The isotherms for the final steady state that appeared in the experiment in Figure 17. (a) Horizontal cross-section indicating remarkably regular square cell structure; (b) Vertical cross-section along the diagonal in (a). Note the presence of the thin boundary layers at the top and at the bottom.

at $z = 0, L$). The initial disturbance was chosen to be 2D, and the 3D computer noise did not affect the heat flux until $t > 100$, at which time a transition to a steady 3D pattern (Fig. 18a,b) with a square planform occurred.[4] The final values of the heat flux and flux ratio were

$$Nu = 15, \qquad \gamma = 0.90, \qquad \mu = 1/40.$$

4. Similar 3D patterns were obtained for smaller μ, but stable 2D patterns were obtained for larger μ. Note that in the lab experiments (referred to below) μ is not an independent parameter, but is determined by the overall $T$, $S$ differences.

In addition to reducing $Nu$ by more than an order of magnitude from its value in the unbounded model, the rigid solution has thin boundary layers at $z = 0, L$ (Fig. 18b) and modified mean fields such that the local density ratio at $z = L/2$ increases to 2.4, as compared with the overall $R = 1.6$.

This value of $\gamma$ compares favorably with $\gamma = 0.88$ obtained by Griffiths and Ruddick (1980) in their "run-down" experiment. Their nondimensional heat flux is given by

$$Nu = \frac{\gamma F_S}{\kappa_T \Delta T/L} = \frac{\gamma (C/\rho)(\Delta S)^{4/3}}{\kappa_T \Delta T/L} = \frac{\gamma (C/\rho)(\Delta T)^{1/3} L}{R^{4/3}\kappa_T}$$

where $\rho \equiv 1.05$ g/cc, $\Delta T$ equals the overall difference in $T$ between the two deep mixed layers, $R = \Delta T/\Delta S$, and their expansion coefficients have been absorbed in our $S$, $T$ symbols. For $R = 1.6$ their Figure 4 gives

$$C \approx 0.3 \times 10^{-3} \text{ g cm}^{-2}\text{s}^{-1},$$

and from their Figure 5b we estimate $L \approx 2.4$ cm. The *initial* $\Delta T$ for this run was $1.7 \times 5.8\%$, and we estimate at the time of Figure 5b the value of $\Delta T$ is reduced by half, or $\Delta T$ $1.7 \times 0.058/2 = 0.049$ (n.b. $Nu$ only depends on $(\Delta T)^{1/3}$).

To estimate the experimental aspect ratio $\mu$ we turn to Figure 19 in Shirtcliffe and Turner (1970), which at $L = 2.4$ cm gives a finger half width of 0.13/2, or $\mu = (0.13/2)/2.4 = 1/37$, which is close to the value (1/40) used in our calculation. Based on an overall $R = 1.6$ we then get

$$Nu = \frac{(0.88)(0.3/1.05)10^{-3}(0.049)^{1/3}(2.4)}{(1.6)^{4/3}(1.5 \times 10^{-5})} = 7.9$$

which is half the value in our rigid lid model. Lambert and Demenkow (1972, p. 639) have found "for a typical experiment $F_S(k_S \Delta S/L)^{-1}$ is of the order of 50." Therefore, $Nu = 50\ \tau\gamma/R \approx 50(1/3)(0.88)/1.6 = 9$. Although the appropriate $R$ is uncertain in this experiment, the flux is consistent with Griffiths and Ruddick (1980), and consistent with our model containing a rather strong rigid boundary condition.

## 7. Conclusions and suggestions

For small aspect ratio ($\mu$) two-dimensional salt fingers are highly unstable to three-dimensional perturbations, and the latter have statistically steady values of the convective heat flux $Nu \equiv -\langle \overline{wT} \rangle$ and temperature variance $\langle \overline{T^2} \rangle$ which are much larger than those in the *two-dimensional* case (SR). The unconstrained two-dimensional calculations may be of interest only when a strong external shear (Kunze, 1994) is present.

All of the simulations in the *unconstrained* 3D regime are characterized by dominant vertical ($m = 0$) mode, whose nonlinear equilibration is due to the relatively small amplitude ("round eddies") modes with vertical scale comparable to the fingerwidth; these eddies absorb energy from the $m = 0$ mode *via* the classical "triad mode interaction"

mechanism. The convective modification of the horizontally averaged $T$, $S$ fields is small, and has an insignificant nonlinear stabilization effect. In the $(R, \tau)$ range considered the statistical averages of heat flux and temperature variance were found to be insensitive to the increase of the fundamental vertical wavelength, indicating convergence of these averages, and validating the vertically *unbounded* model.

Most of our calculations concentrated on the parameters $\tau = 1/3$, $R = 2.8$, and the extension to $1.8 \leq R \leq 2.6$ (Section 4) showed that the finger structure is similar. The flux values are summarized in Table 2, and Eq. (4.1) gives the approximate empirical formulas for the statistically averaged values of the heat flux, density flux and the temperature variance as functions of $\varepsilon$ (for $0.07 < \varepsilon < 0.88$). For smaller values the asymptotic $(\varepsilon \to 0)$ $(R \to 1/\tau)$ theory (Section 5) is qualitatively useful in verifying and understanding the mechanism of nonlinear stabilization.

Although past laboratory experiments involve intractable boundary conditions, an approximation to these (Section 6) yields very good agreement for the flux ratio $\gamma$, and the individual fluxes agree within a factor of two. Nevertheless it is suggested that future experiments be made to test the unbounded model, which gives the flux (or the horizontal variances) as a function of the local average $T$-$S$ gradients.

*Acknowledgments.* We gratefully acknowledge the financial support for this work provided by the National Science Foundation under grants OCE-9216319, OCE-9529261 and OCE-9726584.

## APPENDIX

### A rigorous demonstration of the 3D instability of steady 2D rolls

An exact steady 2D equilibrium state (as well as an exact 3D state) with vertical velocities satisfying "rigid" boundary conditions $w = 0$ at $z = 0, L$ can be obtained numerically in terms of a Fourier sine series for $(T, S)$ (excluding all cosine terms, including $m = 0$). We made such calculations with the 3D code for $\mu = 0.2$ and for parameters $(\tau, R, \Delta x, \Delta y, \Delta t, \ldots)$ corresponding to those in Section 2. The resulting steady temperature field (Fig. 19a) normal to the rolls is the same as obtained by SR using a 2D code. We now want to show that this true *equilibrium* is *linearly* unstable when all Fourier components (including cosine terms) are allowed as perturbations in the 3D code. The fastest growing normal mode was computed as follows.

The system (2.1) was linearized about the steady state $\{T^*, S^*, \mathbf{v}^*\}$ to obtain

$$\begin{cases} 0 = -\nabla\hat{p} + \nabla^2\hat{\mathbf{v}} + (\hat{T}' - \hat{S}')k, \\ \nabla \cdot \hat{\mathbf{v}} = 0 \\ \dfrac{\partial}{\partial t}\hat{T} + \nabla \cdot (\hat{\mathbf{v}}T^*) + \nabla \cdot (\mathbf{v}^*\hat{T}) + \hat{w} = \nabla^2\hat{T} \\ \dfrac{\partial}{\partial t}\hat{S} + \nabla \cdot (\hat{\mathbf{v}}S^*) + \nabla \cdot (\mathbf{v}^*\hat{S}) + \dfrac{1}{R}\hat{w} = \tau\nabla^2\hat{S} \end{cases} \tag{A.1}$$

where $\{\hat{T}, \hat{S}, \hat{\mathbf{v}}\}$ is a small 3D disturbance. These equations were numerically integrated using Figure 19a for $\{T^*, S^*, \mathbf{v}^*\}$. The pseudo-spectral method used to compute $\{\hat{T}, \hat{S}, \hat{\mathbf{v}}\}$ is

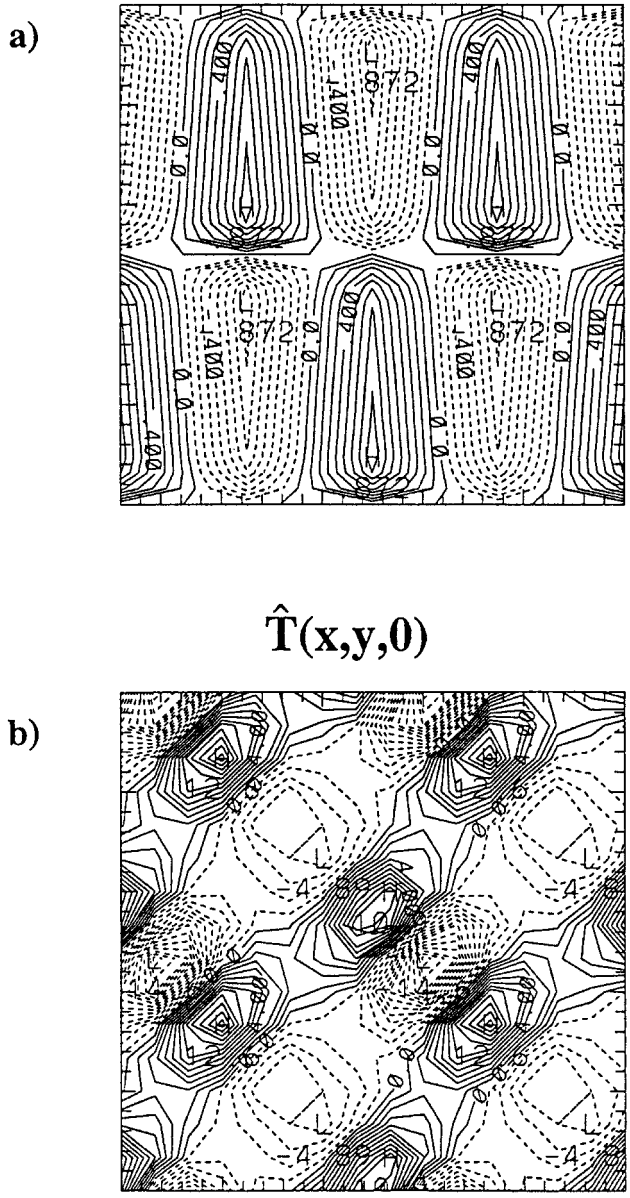


Figure 19. (a) The experiment with the *rigid lid* code initiated by "rolls" (Eq. 2.2) with aspect ratio 1:5 yields a steady state as given by the vertical cross-section of temperature ($T^*$), in the direction normal to the orientation of the "rolls." (b) Isotherms $\hat{T}(x, y, 0)$ of the fastest growing disturbance at z = 0 (for the steady state consisting of the 2D rolls in Fig. 19a). This disturbance can be associated with "rolls" oriented *normal* to the basic state rolls.

similar to the one used in Sections 2–5, and corresponds to the *unconstrained* system without subharmonics (i.e., the horizontal size of the computational domain equals the wavelength of the fastest growing mode (2.4)). The fastest growing normal mode was obtained by introducing a norm of the disturbance $a = \langle \overline{\hat{T}^2} \rangle^{1/2}$, and computing it at fixed intervals of time $t_{int}$. When calculations were initiated by a random initial condition for $(\hat{T}, \hat{S})$ after a while the norm "$a$" started to increase by equal amounts:

$$\lim_{t\to\infty} \frac{\mathrm{a}(t + t_{\mathrm{int}})}{a(t)} = \mathrm{const} = \exp(\lambda t_{int}). \tag{A.2}$$

This means that the disturbance is eventually dominated by the fastest growing normal mode, and Figure 19b shows the temperature eigenfunctions in the regions $z = 0, L$ of strong gradients. These perturbations may be described as (mainly) secondary rolls aligned *normal* to the basic field rolls. The growth rate $\lambda = 0.039$ is an order of magnitude larger than the maximum growth rate (0.0036) of the primary instability in a completely *undisturbed* initial state with uniform vertical gradients. This indicates that the energy for this secondary instability is mostly supplied by the large local mean field gradients of the steady state in the boundary layers (see Fig. 19a) rather than by the basic $(\overline{T}, \overline{S})$ gradient. Especially noteworthy is the fact that the fastest growing perturbation of these 2D solutions is fundamentally three-dimensional.

## REFERENCES

Canuto, C., M. Y. Hussaini, A. Quarteroni and T. A. Zang. 1987. Spectral Methods in Fluid Dynamics, Springer Series in Computational Physics, Springer-Verlag, 567 pp.

Griffiths, R. W. and B. R. Ruddick. 1980. Accurate fluxes across a salt-sugar finger interface deduced from direct density measurements. J. Fluid Mech., *99,* 85–95.

Kunze, E. 1994. A proposed flux constraint for salt fingers in shear. J. Mar. Res., *52,* 999–1016.

Lambert, R. B. and J. W. Demenkow. 1972. On vertical transport due to fingers in double diffusive convection. J. Fluid. Mech., *54,* 627–640.

Proctor, M. R. E. and J. Y. Holyer. 1986. Planform selection in salt fingers. J. Fluid Mech., *168,* 241–253.

Shirtcliffe, T. G. L. and J. S. Turner. 1970. Observations of the cell structure of salt fingers. J. Fluid Mech. *41,* 707–719.

Stern, M. E. and T. Radko. 1998. The salt finger amplitude in unbounded T-S gradient layers. J. Mar. Res., *56,* 157–196.

Stern, M. and J. S. Turner. 1969. Salt fingers and convecting layers. Deep-Sea Res., *16,* 497–511.

Turner, J. S. and C. F. Chen. 1974. Two-dimensional effects in double-diffusive convection. J. Fluid Mech., *63,* 577–592.

Received: *11 August, 1998;* revised: *14, January, 1999.*